Inverse scattering for optical coherence tomography

Tyler S. Ralston, Daniel L. Marks, P. Scott Carney, and Stephen A. Boppart

Beckman Institute for Advanced Science and Technology, Department of Electrical and Computer Engineering, University of Illinois at Urbana-Champaign, Urbana, Illinois 61801

Inverse scattering theory for optical coherence tomography (OCT) is developed. The results are used to produce algorithms to resolve three-dimensional object structure, taking into account the finite beam width, diffraction, and defocusing effects. The resolution normally achieved only in the focal plane of the OCT system is shown to be available for all illuminated depths in the object without moving the focal plane. Spatially invariant resolution is verified with numerical simulations and indicates an improvement of the high-resolution cross-sectional imaging capabilities of OCT. © 2006 Optical Society of America

OCIS codes: 170.4500, 110.6960, 110.6880, 110.1650, 100.6950, 100.6890.

1. BACKGROUND AND INTRODUCTION

Optical microscopy has long relied on the design of physical optical elements to produce images of samples. However, with the advent of scanning modalities such as confocal microcopy, near-field scanning optical microscopy, and optical coherence tomography (OCT), image quality is determined as much by algorithm development as the quality of optical elements. Data synthesis and image formation algorithms have been crucial in other nonoptical imaging modalities such as synthetic aperture radar (SAR) where improved algorithms have dramatically increased the performance of such systems. For example, the modeling of physical parameters has led to enhanced modes of strip-map and spotlight SAR imaging.[1,2]

OCT is a high-resolution noncontact optical imaging modality that can image highly scattering tissues at depths of up to 3 mm, depending on the tissue type. It is a range-finding technique that relies on optical scattering in biological specimens to form micrometer-scale cross-sectional images.[3–5] Maintaining a relatively uniform resolution within the sample has been a concern, since apparent morphology affects the way an object is categorized. For example, a biological specimen with precancerous cellular changes may go unnoticed if the cellular precursors lie in an imaging region having a reduced resolution,[6,7] and a nonuniform resolution may result in misdiagnosis.[8]

In OCT, optical hardware such as adaptive optics or axicon lenses have been utilized to increase the transverse resolution over a large range of depths in a specimen.[9,10] Such optical techniques and hardware can help generate images with high transverse resolution over relatively large scanning depths. Dynamic focusing or focus tracking is useful for *en face* imaging, imaging in planar sections, with optical coherence microscopy,[4,11] or for cross-sectional imaging, where the tight focus is scanned at some depth in the specimen.[12] Dynamic focusing techniques in a system design may require specific hardware modifications that can be difficult to control in

real time. Some authors have designed algorithms that improve the axial resolution by compensating for the nonlinear dispersion between data in the temporal domain and the spatial domain.[13–15] Of these methods, some are used to correct for the limited bandwidth of the laser spectrum, while others correct for the dispersion induced by the optical system or the specimen. However, modeling of the physical processes has been limited to a one-dimensional quasi-monochromatic model.[16,17] These models do not take into account the relationship between data acquired at different transverse positions of the beam, the finite transverse extent of the beam, or properties of the medium. Others have tried to correct for artifacts produced by refraction, sample positioning, and the scanning procedure.[18] Furthermore, some authors have detailed a theoretical model of OCT including a lens and a heterodyning model.[19]

In this paper, we develop a mathematical model connecting the acquired OCT signal with the three-dimensional object structure, taking into account the finite beam width and focusing. We then solve an inverse scattering problem and determine the structure of the imaged object from the data available. In solving the inverse problem, we compensate for spectrum-limited resolution in the axial direction as well as the Gaussian beam blurring in an optimal (least-squared error) sense.

2. DESCRIPTION OF OPTICAL COHERENCE TOMOGRAPHY

In OCT, a narrow, well-collimated beam of light is directed into a sample. The returned, or backscattered, light is collected. The time of flight to scatterers within the sample is determined by coherence gating the returned signal. A Michelson interferometer is used to measure temporal coherence in a time-domain OCT system; see Fig. 1(a). The light arriving at a photodetector shifts between states of constructive and destructive interference when the mirror in the reference arm is displaced.
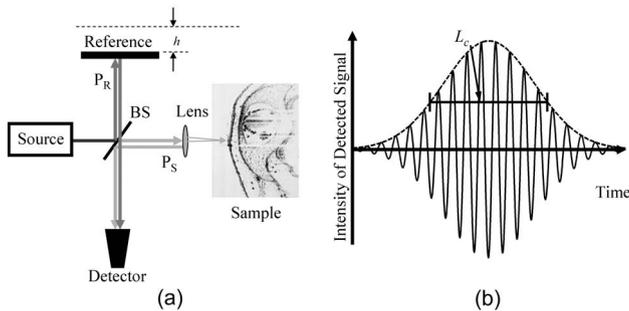
Fig. 1. (a) Typical Michelson interferometer for use in OCT. BS is the beam splitter, P_S is the sample path, P_R is the reference path, and h is the distance traveled by the reference mirror. (b) Interferogram of an impulse response for an OCT system with a low-coherence source having a Gaussian spectrum and a full width at half-maximum (FWHM) coherence length L_c.
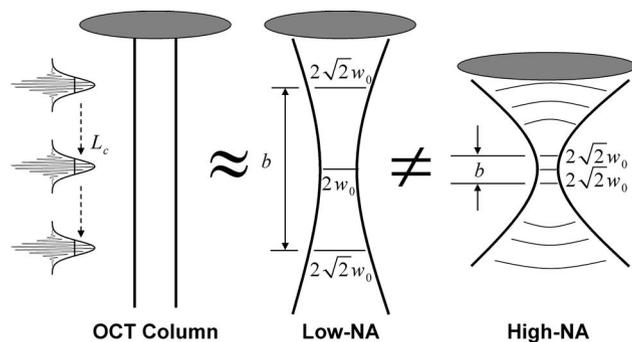

Fig. 2. Geometry of a Gaussian beam for low- and high-numerical-aperture (NA) lenses. These geometries are contrasted with the assumption of a collimated axial OCT scan. b is the confocal parameter, w_0 is the beam radius at the focus, and L_c is the coherence length of the source.

The collected signal is an interferogram, i.e., the cross-correlation signal, or the intensity versus difference in reference and sample path lengths, and is given by the expression

$$S(\mathbf{r}_0,t) = \int dt' E_r(t') E_s^*(\mathbf{r}_0,t'-t), \qquad (2.1)$$

where $E_r(t)$ and $E_s(\mathbf{r}_0,t)$ are the reference and sample electromagnetic fields in a scalar model for the received signal $S(\mathbf{r}_0,t)$. An interferogram for a single perfect reflector, such as a mirror, is displayed in Fig. 1(b).

The envelope of the interferogram is the point response function in the axial direction of the system and corresponds directly to the axial resolution of the system. Axial resolution is directly proportional to the optical coherence length of the light and thus inversely proportional to the spectral bandwidth of the source. It is often convenient to work with the Fourier transform of Eq. (2.1) with respect to time, which is given by

$$S(\mathbf{r}_0,\omega) = E_r(\omega) E_s^*(\mathbf{r}_0,\omega). \qquad (2.2)$$

This signal $S(\mathbf{r}_0,\omega)$ can be measured directly using spectral-domain OCT.[20,21]

The sample under investigation may be known to consist of a semitransparent background with an index of re-

fraction n. In the medium then, the wavenumbers k are related to the frequencies ω by the dispersion relation $k(\omega) = \omega n/c$. It will be advantageous to work with data that are a function of k rather than ω. To preserve energy content of the signal, the data must also be multiplied by the Jacobian of the transformation,

$$S_k(\mathbf{r},k) = S_\omega(\mathbf{r},\omega)(\partial k/\partial \omega)^{-1}. \qquad (2.3)$$

OCT images are formed by assembling adjacent low-numerical-aperture axial scans to generate two-dimensional, cross-sectional images.[4,5] Figure 2 illustrates the common assumption among OCT researchers that the low-numerical-aperture lens is a tool for generating collimated planar wavefronts. This assumption neglects the characteristics of the incident Gaussian beam. Therefore a standard OCT system will exhibit transverse resolution that is not constant, but depends on depth and the focal properties of the lens. This apparent loss of resolution, or distortion, does not necessarily result in a loss of signal power. By characterizing this distortion, it is possible to correct it and produce images that are commensurate with ideal beam collimation. Lenses of a higher numerical aperture (NA) are able to focus a beam to a relatively smaller spot size in the focal plane. However, high-NA lenses produce a more pronounced distortion of features out of the focal plane. Hence, high-NA lenses are good for optical sectioning in parallel planes (*en face*) such as in multiphoton or confocal microscopy.[22] Lenses with a lower NA are usually used for OCT imaging, since they produce a relatively uniform transverse resolution over the axial (depth) scan. Furthermore, the confocal parameter of the lens (distance around the focus where the beam profile has a relatively uniform width) is generally chosen to closely match the penetration depth of a particular type of tissue.

Many OCT images exhibit poor transverse resolution outside of the confocal region, manifested as curved and blurred features imaged in those areas. If a relatively high-NA objective is used, where the axial scan length exceeds the length of the confocal region (twice the Rayleigh range), then there is a more pronounced apparent loss of transverse resolution outside of the confocal region. The goal of this work is to digitally reduce the distortion outside of the confocal region by solving the inverse problem based on the physics of the scattering process. By solving the inverse problem we are able to produce images with more sharply defined features. More importantly, the solution resolves closely adjacent scatterers, even those that produce interference in the raw OCT image. This is a crucial advantage of inverse scattering over simple deconvolution of a real-valued point-spread function.

3. MATHEMATICAL DESCRIPTION OF THE EXPERIMENT

As discussed in the previous section, to simplify the model for OCT data acquisition, several assumptions are generally made about an OCT system. These assumptions do not take into account the shape of wavefronts produced by lens optics, the spectrum of the source, or unbalanced dispersion in the media. The ideal instrument produces a perfectly collimated beam of zero width at every point in

the sample. However, real instruments produce a field more accurately described as a Gaussian beam of finite waist size and divergence.

We assume a linear relationship between the sample susceptibility η and the measured signal S:

$$S = K\eta, \tag{3.1}$$

where K is an operator characterizing the OCT system. Such a linear model is implicitly the result of taking the first Born approximation for the scattering. OCT is especially amenable to the first Born approximation since contributions from multiple scattering will tend to be delayed by a longer time and thus may fall outside the coherence time of the reference. As depths of penetration increase, contributions from multiple scattering in the shallow region increase.

As previously discussed, there will exist a nontrivial relationship between frequencies ω and real-valued wavenumbers k in the sample described by a dispersion relation $\omega = kc/n(\omega)$. Moreover, the field produced by the source is an ergodic random process with power spectral density $A^2(k)$. $A(k)$ is assumed to be band-limited such that $0 < k_{min} < k < k_{max}$. The signal S is understood to be the result of ensemble averaging over all realizations of the source. In each realization of the source, the beam projected into the sample is Gaussian and at each frequency has beam waist W_0 given by the expression

$$W_0(k) = \frac{\alpha}{k}, \tag{3.2}$$

where $\alpha = \pi/\text{NA}$, and NA is the numerical aperture of the output lens of the system (see Fig. 3). The normalized beam profile in the waist plane is given by the expression

$$g_0(\mathbf{r}, k) = \frac{1}{2\pi W_0^2(k)} e^{-r^2/(2W_0^2(k))}, \tag{3.3}$$

where $\mathbf{r}$ is the position vector transverse to the beam axis. The beam, displaced by a vector $\mathbf{r}_0$, may be written in terms of the plane-wave decomposition with transverse spatial-frequency coordinates $\mathbf{q}$,

$$g(\mathbf{r}' - \mathbf{r}_0, k) = \frac{1}{(2\pi)^2} \int d^2q \ e^{i\mathbf{q}\cdot(\mathbf{r}'-\mathbf{r}_0)} \widetilde{g}(\mathbf{q}, z' - z_0, k), \tag{3.4}$$

where

$$\widetilde{g}(\mathbf{q}, z, k) = e^{ik_z(\mathbf{q})z} \widetilde{g}_0(\mathbf{q}, k), \tag{3.5}$$

$$k_z(\mathbf{q}) = \sqrt{k^2 - q^2}, \tag{3.6}$$

$$\widetilde{g}_0(\mathbf{q}, k) = e^{-q^2(W_0^2(k))/2} = e^{-q^2(\alpha^2/2k^2)}. \tag{3.7}$$

We exclude surface effects with the use of a coherence gate. The backscattered field in the first Born approximation is given by the expression

$$U(\mathbf{r}, \mathbf{r}_0, k) = A(k) \int_V d^3r' G(\mathbf{r}', \mathbf{r}, k) g(\mathbf{r}' - \mathbf{r}_0, k) \eta(\mathbf{r}'), \tag{3.8}$$

where $\mathbf{r}_0$ is the transverse position of the beam, $G(\mathbf{r}', \mathbf{r}, k)$ is the free-space form of the Green's function.

The signal $S(\mathbf{r}_0, k)$ coupled back into the fiber is derived in Appendix A and is given by

$$S(\mathbf{r}_0, k) = \int_\Sigma d^2r \, U(\mathbf{r}, \mathbf{r}_0, k) g(\mathbf{r} - \mathbf{r}_0, k), \tag{3.9}$$

where Σ is the aperture in the output plane of the optical system.

Substituting Eq. (3.8) for $U(\mathbf{r}, \mathbf{r}_0, k)$, we obtain

$$S(\mathbf{r}_0, k) = A(k) \int_\Sigma d^2r \int_V d^3r' G(\mathbf{r}', \mathbf{r}, k) g(\mathbf{r}' - \mathbf{r}_0, k) \eta(\mathbf{r}')$$
$$\times g(\mathbf{r} - \mathbf{r}_0, k). \tag{3.10}$$

The photodetector measures the interferometric cross correlation between the reference and sample signals as a function of the relative time delay between the two, as described in Section 2. The reference field is well characterized and so S may be determined from the measurements. Thus it is assumed that S is the observable.

The forward problem may be cast such that K in Eq. (3.1) takes a diagonal form. The Green's function $G(\mathbf{r}', \mathbf{r}, k)$ may be written as a superposition of plane waves,

$$G(\mathbf{r}', \mathbf{r}, k) = \frac{1}{(2\pi)^2} \int d^2q \ e^{i\mathbf{q}\cdot(\mathbf{r}-\mathbf{r}')} \widetilde{G}(\mathbf{q}, z - z', k). \tag{3.11}$$

Without loss of generality, we take $z = 0$ to be the measurement plane. Taking the Fourier transform of $S(\mathbf{r}_0, k)$ with
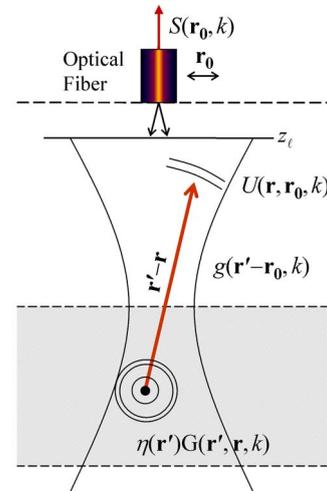

Fig. 3. (Color online) Illustration of the notation and relation to the scattering and measurement process. The field emerges from the fiber and is projected by a thin lens in the $z = z_\ell$ plane to produce a beam with normalized profile $g(\mathbf{r}' - \mathbf{r}_0, k)$. The field interacts with the sample to produce, from each point $\mathbf{r}'$ in the sample, a scattered field $U(\mathbf{r}, \mathbf{r}_0, k) = \eta(\mathbf{r}')G(\mathbf{r}', \mathbf{r}, k)$. This field is then collected and projected back into the fiber to produce the signal $S(\mathbf{r}_0, k)$.

respect to the transverse components of $\mathbf{r}_0$, with spatial-frequency coordinates $\mathbf{Q}$ such that $S(\mathbf{r}_0, k) = (2\pi)^{-2} \int d^2 Q \, e^{i\mathbf{Q}\cdot\mathbf{r}_0} \widetilde{S}(\mathbf{Q}, z_0, k)$, yields

$$\widetilde{S}(\mathbf{Q}, z_0, k) = A(k) \int d^2 q \int dz' e^{ik_z(\mathbf{q}+\mathbf{Q})(z'-z_0)} e^{-ik_z(\mathbf{q})z_0}$$

$$\times \widetilde{G}(\mathbf{q}, -z', k) \widetilde{g}_0(\mathbf{q}+\mathbf{Q}, k) \widetilde{g}_0(-\mathbf{q}, k) \widetilde{\eta}(\mathbf{Q}; z'), \quad (3.12)$$

where $\widetilde{\eta}(\mathbf{q}; z)$ is the Fourier transform of η with respect to the transverse components of $\mathbf{r}$. The angular spectrum amplitude of the free-space Green's function is given by the expression[23]

$$\widetilde{G}(\mathbf{q}, z - z', k) = \frac{i2\pi}{k_z(\mathbf{q})} e^{-ik_z(\mathbf{q})(z-z')}, \quad (3.13)$$

with $k_z(\mathbf{q})$ given by Eq. (3.6). The signal coupled back into the fiber now becomes

$$\widetilde{S}(\mathbf{Q}, k) = A(k) \int d^2 q \int dz' \frac{i2\pi}{k_z(\mathbf{q})} e^{ik_z(\mathbf{q})z'} e^{ik_z(\mathbf{q}+\mathbf{Q})(z'-z_0)} e^{-ik_z(\mathbf{q})z_0}$$

$$\times \widetilde{g}_0(\mathbf{q}+\mathbf{Q}, k) \widetilde{g}_0(-\mathbf{q}, k) \widetilde{\eta}(\mathbf{Q}; z'). \quad (3.14)$$

Notice that $k_z(\mathbf{q})$ is an even symmetric function so that $k_z(\mathbf{q}) = k_z(-\mathbf{q})$. By separating terms and transforming $\mathbf{q} \leftrightarrow -\mathbf{q}$, the relation may be expressed as

$$\widetilde{S}(\mathbf{Q}, k) = A(k) \int d^2 q \int dz' \frac{i2\pi}{k_z(\mathbf{q})} e^{ik_z(\mathbf{q})(z'-z_0)} \widetilde{g}_0(\mathbf{q}, k)$$

$$\times e^{ik_z(\mathbf{Q}-\mathbf{q})(z'-z_0)} \widetilde{g}_0(\mathbf{Q}-\mathbf{q}, k) \widetilde{\eta}(\mathbf{Q}; z'). \quad (3.15)$$

The signal may now be written more compactly as

$$\widetilde{S}(\mathbf{Q}, k) = i2\pi A(k) \int dz' H(\mathbf{Q}, z', k) \widetilde{\eta}(\mathbf{Q}; z'), \quad (3.16)$$

where

$$H(\mathbf{Q}, z, k) = \int d^2 q \, k_z^{-1}(\mathbf{q}) e^{ik_z(\mathbf{q})(z-z_0)} \widetilde{g}_0(\mathbf{q}, k)$$

$$\times e^{ik_z(\mathbf{Q}-\mathbf{q})(z-z_0)} \widetilde{g}_0(\mathbf{Q}-\mathbf{q}, k). \quad (3.17a)$$

In the paraxial approximation, the factor $1/k_z(\mathbf{q}) \approx 1/k$ so that the following simplification is made:

$$H(\mathbf{q}, z, k) = k^{-1}(\widetilde{f} * \widetilde{f})(\mathbf{q}, z, k), \quad (3.17b)$$

where $\widetilde{f}(\mathbf{q}, z, k) = e^{ik_z(\mathbf{q})(z-z_0)} \widetilde{g}_0(\mathbf{q}, k)$, and $*$ denotes convolution in $\mathbf{q}$.

Using Parseval's theorem, Eq. (3.16) reduces to a relatively simple relationship,

$$S(\mathbf{r}_0, k) = i2\pi A(k) k^{-1} \int d^3 r \, f(\mathbf{r} - \mathbf{r}_0, k)^2 \eta(\mathbf{r}), \quad (3.18)$$

where

$$f(\mathbf{r}, k) = (2\pi)^{-2} \int d^2 q \, e^{i\mathbf{q}\cdot\mathbf{r}} \widetilde{f}(\mathbf{q}, z, k). \quad (3.19)$$

Making use of Eq. (3.7) we find that

$$\widetilde{f}(\mathbf{q}, z, k) = e^{i(z-z_0)\sqrt{k^2-q^2}} e^{-q^2(\alpha^2/2k^2)}. \quad (3.20)$$

Additionally, in the Fresnel zone, when $k_{\min} \gg q$, the approximation for the phase can be used:

$$\sqrt{k^2 - q^2} \approx k - \frac{1}{2}\frac{q^2}{k}, \quad (3.21)$$

so that

$$\widetilde{f}(\mathbf{q}, z, k) = e^{i(z-z_0)k} e^{-q^2(\alpha^2/2k^2 + i(z-z_0)/2k)}. \quad (3.22)$$

Thus the kernel H takes the form

$$H(\mathbf{Q}, z, k) = (\widetilde{f} * \widetilde{f})(\mathbf{Q}, z, k)$$

$$= \frac{1}{4\pi}\left(\frac{\alpha^2}{k^2} + i\frac{(z-z_0)}{k}\right)^{-1}$$

$$\times e^{2i(z-z_0)k} e^{-Q^2/2(\alpha^2/2k^2 + i(z-z_0)/2k)}. \quad (3.23)$$

Equation (3.16) may be seen to be a type I Fredholm integral equation[24] and the kernel of the operator K is apparent:

$$\widetilde{S}(\mathbf{Q}, k) = i2\pi A(k) \int dz' d^2 Q' \delta^{(2)}(\mathbf{Q} - \mathbf{Q}')$$

$$\times H(\mathbf{Q}', z', k) \widetilde{\eta}(\mathbf{Q}'; z'). \quad (3.24)$$

Substituting $\widetilde{\eta}(\mathbf{Q}'; z') = (1/2\pi) \int d\beta \, e^{i\beta z'} \widetilde{\widetilde{\eta}}(\mathbf{Q}'; \beta)$, we obtain a representation for K:

$$\widetilde{S}(\mathbf{Q}, k) = K\widetilde{\eta}(\mathbf{Q}'; \beta) = iA(k) \int d\beta d^2 Q' \delta^{(2)}(\mathbf{Q} - \mathbf{Q}')$$

$$\times \widetilde{H}(\mathbf{Q}', -\beta, k) \widetilde{\widetilde{\eta}}(\mathbf{Q}'; \beta), \quad (3.25)$$

where $\widetilde{H}(\mathbf{Q}, \beta, k) = (k/2) e^{-iz_0\beta} e^{\alpha^2/k(\beta-2k)} u(-\beta + 2k - Q^2/4k)$. The Heaviside unit step function is denoted by $u(\beta) = \{^1_0 \; ^{\beta>0}_{\beta\leq0}$.

4. INVERSE PROBLEM

It may be seen in Eq. (3.25) that the Fourier transform of the observed signal is simply related to the Fourier transform of the object. Thus it might be expected that the object structure may be simply recovered. However, the observed signal will generally be noisy, band limited, and sampled. Generally the inverse problem is ill-conditioned, and possibly ill-posed. Thus K^{-1} is not expected to exist. Rather than find a solution of $S = K\eta$ for η, a suitable substitute, the minimum norm solution of the least-squared error problem, will be accepted. That is, an approximate solution will be sought η^+ that is the minimum norm minimize of $\|S - K\eta^+\|^2$, where $\|\cdot\|$ denotes the $L_2(\mathbb{R}^2)$ or $l_2(\mathbb{R}^2)$ norm, whether the data are continuous or discrete, respectively. This solution may be written

$$\eta^+ = (K^*K)^{-1}K^*S = K^+S, \quad (4.1)$$

where K^+ is the pseudoinverse of K, K^* is the adjoint of K, and K^*K is the normal operator. In the likely event that the normal operator K^*K has a nontrivial null space, $(K^*K)^{-1}$ is understood to be the inverse of K^*K restricted

to the orthogonal complement to the null space. For this particular problem, it will be seen that the normal operator is approximately diagonal so that K^*S gives a very good (qualitative) estimate of η and $(K^*K)^{-1}$ acts merely as a filter. It is thus useful to define the quantity η_A, the unfiltered reconstruction, such that

$$\eta_A = K^*S. \tag{4.2}$$

From Eq. (3.25) it may be seen that

$$\tilde{\eta}_A(\mathbf{Q}'';\beta') = -i \int dk\, d^2Q\, \delta^{(2)}(\mathbf{Q} - \mathbf{Q}'')A(k)$$

$$\times \tilde{H}^*(\mathbf{Q}, -\beta', k)\tilde{S}(\mathbf{Q}, k). \tag{4.3}$$

The normal operator, whose inverse acts as a filter, may be constructed from Eq. (3.25) and its kernel is given by the expression

$$K^*K(\mathbf{Q}',\beta,\mathbf{Q}'',\beta') = \int dk\, A(k)^2\tilde{H}^*(\mathbf{Q}', -\beta, k)$$

$$\times \tilde{H}(\mathbf{Q}'', -\beta', k)\delta^{(2)}(\mathbf{Q}' - \mathbf{Q}''). \tag{4.4}$$

Thus an exact solution for the kernel is given by

$$K^*K(\mathbf{Q}',\beta,\mathbf{Q}'',\beta') = \frac{1}{4} \int dk\, A^2(k)k^2 e^{iz_0(\beta'-\beta)}e^{-\alpha^2/k(\beta'+\beta+4k)}$$

$$\times u\left(\beta' + 2k - \frac{Q''^2}{4k}\right)u\left(\beta + 2k - \frac{Q'^2}{4k}\right)$$

$$\times \delta^{(2)}(\mathbf{Q}' - \mathbf{Q}''). \tag{4.5}$$

In practice, the operators K^* and K^*K as specified by Eqs. (4.3) and (4.5), while accurate to the extent of the approximations made, do not have sparse kernels. Thus computing the pseudoinverse, Eq. (4.1) will require computationally intensive numerical evaluation of $(K^*K)^{-1}$. In certain cases, great simplification can be achieved by evaluating Eq. (4.5) approximately.

A. Thin Samples
As noted above, K^*K may be difficult to invert. When the sample is thin, specifically when the sample thickness is small compared to α^2/k, an important simplification may be achieved. The expression for $H(\mathbf{Q},z,k)$ in Eq. (3.23) contains a slowly varying factor and a rapidly oscillating factor:

$$H(\mathbf{Q},z,k) = I(\mathbf{Q},z,k)e^{i\phi(\mathbf{Q},z,k)}, \tag{4.6a}$$

where

$$I(\mathbf{Q},z,k) = \frac{1}{4\pi}\left(\frac{\alpha^2}{k^2} + i\frac{(z-z_0)}{k}\right)^{-1}e^{-Q^2/2(\alpha^2/2k^2)} \tag{4.6b}$$

and

$$\phi(\mathbf{Q},z,k) = 2(z - z_0)k - \frac{Q^2(z - z_0)}{4k}. \tag{4.6c}$$

The rapidly oscillating component $e^{i\phi(\mathbf{Q},z,k)}$ accounts for the diffraction of the Gaussian beam, which results in dif-

fraction effects outside of the focal plane. The slowly varying component $I(\mathbf{Q},z,k)$ accounts for the finite NA of the Gaussian beam and the attenuation of the signal outside of the confocal region. If the sample is thin so that the range of $z-z_0$ is much less than α^2/k, then to a good approximation

$$I(\mathbf{Q},z,k) = I_k(\mathbf{Q},k) = \frac{k^2}{4\pi\alpha^2}e^{-Q^2/2(\alpha^2/2k^2)}. \tag{4.6d}$$

Thus $\tilde{H}(\mathbf{Q},-\beta,k)$ reduces to

$$\tilde{H}(\mathbf{Q},-\beta,k) = I_k(\mathbf{Q},k)e^{iz_0\beta}\delta(\beta + 2k - Q^2/4k). \tag{4.7}$$

Thus Eq. (3.25) just becomes

$$\tilde{S}(\mathbf{Q},k) = iA(k) \int d\beta d^2Q'\, \delta^{(2)}(\mathbf{Q} + \mathbf{Q}')I_k(\mathbf{Q},k)$$

$$\times \delta\left(\beta - \left(\frac{Q'^2}{4k} - 2k\right)\right)e^{iz_0\beta}\tilde{\tilde{\eta}}(\mathbf{Q}';\beta), \tag{4.8}$$

and Eq. (4.3) becomes

$$\tilde{\tilde{\eta}}_A(\mathbf{Q}'';\beta') = -i \int dk d^2Q\, \delta^{(2)}(\mathbf{Q} + \mathbf{Q}'')A(k)I_k(\mathbf{Q},k)$$

$$\times \delta\left(k - \frac{1}{2}\left(\frac{\beta'}{2} + \sqrt{\left(\frac{\beta'}{2}\right)^2 + \frac{Q^{*2}}{2}}\right)\right)$$

$$\times \left|2 + \frac{Q''^2}{4k^2}\right|^{-1}e^{iz_0(2k-Q''^2/4k)}\tilde{S}(\mathbf{Q},k). \tag{4.9}$$

The normal operator is diagonal,

$$K^*K(\mathbf{Q}',\beta,\mathbf{Q}'',\beta')$$

$$= \delta^{(2)}(\mathbf{Q}'' - \mathbf{Q}')\delta(\beta - \beta'')$$

$$\times \left|2 + \frac{Q'^2}{4k^2}\right|^{-1}A(k)^2I_k(\mathbf{Q}',k)^2\bigg|_{k=1/2(\beta/2+\sqrt{(\beta/2)^2+Q'^2/2})}, \tag{4.10}$$

so that the pseudoinverse solution, $\eta^+ = K^+S$, is given by the expression

$$\tilde{\tilde{\eta}}^+(\mathbf{Q}',\beta) = \int dk d^2Q\, \delta^{(2)}(\mathbf{Q} + \mathbf{Q}')$$

$$\times \delta\left(k - \frac{1}{2}\left(\frac{\beta}{2} + \sqrt{\left(\frac{\beta}{2}\right)^2 + \frac{Q'^2}{2}}\right)\right)$$

$$\times (A(k)I_k(\mathbf{Q}',k))^{-1}e^{iz_0(2k-Q^2/4k)}\tilde{S}(\mathbf{Q},k). \tag{4.11}$$

B. Narrowband Illumination
An alternate approximation can be made that will result in a sparse kernel, but more accurately accounts for the attenuation of the reconstructed susceptibility away from the focal plane. The factor $I(\mathbf{Q},z,k)$ consists of the product of two terms. The term $(\alpha^2/k^2+i(z-z_0)/k)^{-1}/(4\pi)$ ac-
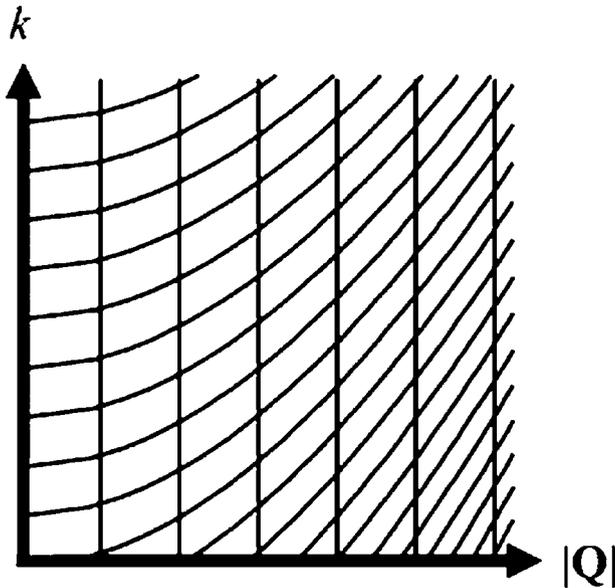
Fig. 4. Sampling lattice of the spatial frequencies in the object space $(\mathbf{Q}, \beta)$ on a uniform grid of the spatial frequencies in the signal space $(\mathbf{Q}, k)$. The curves shown are lines of constant β.

counts for the attenuation (and not the blurring) of the reconstructed object outside of the confocal region. The other term, $e^{-Q^2 \alpha^2/(4k^2)}$, accounts for the transverse resolution by attenuating transverse frequencies (because it is dependent on Q). The calculation is greatly simplified by obtaining a separable form for $I(\mathbf{Q}, z, k)$, where $I(\mathbf{Q}, z, k) = I_z(z) I_k(\mathbf{Q}, k)$. This may be accomplished by setting $(\alpha^2/k^2 + i(z - z_0)/k)^{-1}/(4\pi) \approx (\alpha^2/kk_0 + i(z - z_0)/k)^{-1}/(4\pi)$, where the α^2/k^2 term has been changed to α^2/kk_0 and k_0 is the center frequency of the illumination. Such an approximation is acceptable if the range of k is much smaller than the value of k_0. $I(\mathbf{Q}, z, k)$ may now be factored as indicated with $I_z(z) = (\alpha^2/k_0 + i(z - z_0))^{-1}$ and $I_k(\mathbf{Q}, k) = k \; e^{-Q^2 \alpha^2/(4k^2)}/(4\pi)$. Making use of this approximation, Eq. (3.24) becomes

$$\widetilde{S}(\mathbf{Q}, k) = i2\pi A(k) \int \mathrm{d}z' \mathrm{d}^2 Q' \, \delta^{(2)}(\mathbf{Q} + \mathbf{Q}') I_k(-\mathbf{Q}', k)$$

$$\times [\widetilde{\eta}(\mathbf{Q}'; z') I_z(z')]. \qquad (4.12)$$

Noting that all of the z dependence is in the expression inside the brackets, we now create an alternate definition of $\tilde{\tilde{\eta}}(\mathbf{Q}'; \beta)$ defined implicitly by $\widetilde{\eta}(\mathbf{Q}'; z') I_z(z') = (1/2\pi) \int \mathrm{d}\beta \; e^{i\beta z'} \tilde{\tilde{\eta}}(\mathbf{Q}'; \beta)$. Given this new definition, we find that

$$\widetilde{H}(\mathbf{Q}, -\beta, k) = I_k(\mathbf{Q}, k) e^{iz_0\beta} \delta\left(\beta + 2k - \frac{Q^2}{4k}\right). \quad (4.13)$$

Given this new definition of $\tilde{\tilde{\eta}}(\mathbf{Q}'; \beta)$ and the fact that Eqs. (4.7) and (4.13) are identical, Eqs. (4.8)–(4.10) are the same for both the thin-sample and narrow-bandwidth approximations. Thus, in regions far from the focal plane, we may correct for the signal attenuation by normalizing the reconstructed susceptibility by $I_z(z)$.

Now the action of the pseudoinverse is evident. The adjoint K^* is a backpropagation operator that resamples the data back to the original coordinates in frequency space.

The normal operator K^*K is a space-invariant convolution. Therefore, in principle, the resolution of the reconstructed object should be spatially invariant whether the object is in focus or not in focus.

The operators K and K^* effect a coordinate transformation in the Fourier space. Figure 4 displays the resulting resampling lattice pattern. The unfiltered reconstruction η_A may be obtained from the signal S by interpolated resampling of S from the grid in Fig. 4 back to a Cartesian system.

The resampling scheme described above may be seen as analogous to the Fourier slice theorem. The Fourier slice theorem states that the Radon transform is inverted by resampling Fourier projections from polar to Cartesian coordinates. In a similar manner, the adjoint operator K^* resamples the Fourier space of the projections along the parabolic curves in Fig. 4.

The normal operator K^*K almost certainly will have a null space and small singular values due to the fact that the system does not pass certain frequencies, thus regularization must be used to stabilize the solution. One possibility for regularization is a Tikhonov regularized solution,[25]

$$\hat{\tilde{\tilde{\eta}}} = (K^*K + \lambda L^*L)^{-1} K^* \widetilde{S}, \qquad (4.14)$$

where $\widetilde{S}$ is the OCT signal with noise and the caret denotes the regularized solution. The operator L is chosen to obtain a weighted filter, but may simply be taken to be the identity. Additional details regarding the choice of a regularization parameter are discussed in the following section.

5. NUMERICAL SIMULATION

In this section, the potential of the solution of the inverse scattering problem is explored through numerical simulation. A synthetic object is created as a collection of point-like scatterers. Synthetic forward OCT data are generated from the synthetic object. Gaussian white noise is added to the synthetic OCT data to create a specific signal-to-noise ratio (SNR). In the implementation of the inverse scattering solution, Tikhonov regularization is used to obtain a stable solution as seen in Eq. (4.14). Table 1 summarizes the steps used in this simulation.

In the simulation of the formulated problem, the sample is taken to consist of sub-resolution-sized point scatterers randomly distributed throughout the simulated imaging area of 1024 μm by 1024 μm. An ideal image of the original object can be seen in Fig. 5(a). The

Table 1. Steps in the Simulations Using the Thin-Sample Approximation

1. Construct $\eta(\mathbf{r}_0; z)$.
2. Calculate $S(\mathbf{r}_0, k)$ from $\eta(\mathbf{r}_0; z)$ using Eq. (4.8) (Table 2).
3. Calculate $S_t(\mathbf{r}_0, t)$ from $S_k(\mathbf{r}_0, k)$ using Eq. (2.3) (Table 3).
4. Add Gaussian white noise to $S_t(\mathbf{r}_0, t)$ using Eq. (5.3).
5. Calculate $S_k(\mathbf{r}_0, k)$ from $S_t(\mathbf{r}_0, t)$ using Eq. (2.3) (Table 4).
6. Calculate $\eta_A(\mathbf{r}_0; z)$ from $S(\mathbf{r}_0, k)$ using Eq. (4.9) (Table 5).
7. Calculate $\hat{\eta}(\mathbf{r}_0; z)$ from $\eta_A(\mathbf{r}_0; z)$ using Eq. (4.10) (Table 6).
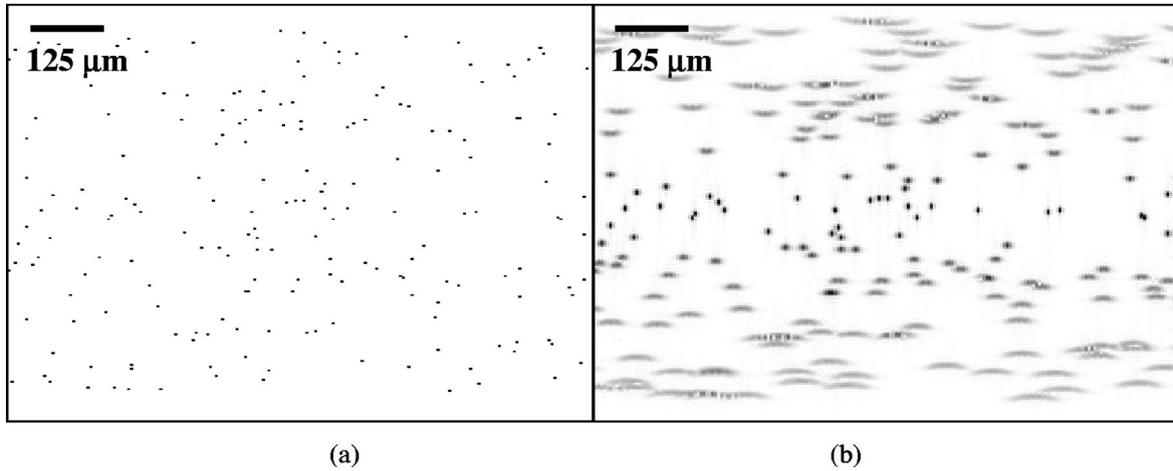
Fig. 5.   (a) Original object model of point scatterers and (b) simulated OCT image with SNR=35 dB.

Table 2. Steps in the Calculation of $S(\mathbf{r}_0, k)$ from $\eta(\mathbf{r}_0; z)$ Using the Thin-Sample Approximation

1. FFT $\eta(\mathbf{r}_0; z)$ along the transverse and axial directions to obtain $\tilde{\eta}(\mathbf{Q}; \beta)$.

2. Interpolate $\tilde{\eta}(\mathbf{Q}; \beta)$, which is spaced uniformly in β using the relation $\beta = Q^2/4k - 2k$, to find samples spaced uniformly in k.

3. Apply a filter, multiplying by $I_k(\mathbf{Q}, k) = k^2/(4\pi\alpha^2)e^{-Q^2\alpha^2/(4k^2)}$ and $iA(k)$ to find $\tilde{S}(\mathbf{Q}, k)$.

4. IFFT $\tilde{S}(\mathbf{Q}, k)$ along the transverse direction $\mathbf{Q}$ to obtain $S(\mathbf{r}_0, k)$.

Table 3. Steps in the Calculation of $S_t(\mathbf{r}_0, t)$ from $S_k(\mathbf{r}_0, k)$

1. Interpolate samples on $S_k(\mathbf{r}_0, k)$ (which is uniformly sampled in k) using the dispersion relation $k(\omega)$ to find $S_\omega(\mathbf{r}_0, \omega)$ $\times[\partial k/\partial \omega]^{-1}$ with samples uniformly spaced in ω.

2. Multiply function $S_\omega(\mathbf{r}_0, \omega)[\partial k/\partial \omega]^{-1}$ with Jacobian $\partial k/\partial \omega$ to find $S_\omega(\mathbf{r}_0, \omega)$.

3. IFFT $S_\omega(\mathbf{r}_0, \omega)$ along the axial direction to find $S_t(\mathbf{r}_0, t)$.

Table 4. Steps in the Calculation of $S_k(\mathbf{r}_0, k)$ from $S_t(\mathbf{r}_0, t)$

1. FFT $S_t(\mathbf{r}_0, t)$ along the axial direction to find $S_\omega(\mathbf{r}_0, \omega)$.

2. Multiply $S_\omega(\mathbf{r}_0, \omega)$ with Jacobian $(\partial k/\partial \omega)^{-1}$ to find $S_\omega(\mathbf{r}_0, \omega)$ $(\partial k/\partial \omega)^{-1}$.

3. Interpolate samples on $S_\omega(\mathbf{r}_0, \omega)$ $(\partial k/\partial \omega)^{-1}$ (which is uniformly sampled in ω) using the dispersion relation $k(\omega)$ to find samples of $S_k(\mathbf{r}_0, k)$, which is uniformly spaced in k.

source spectrum $A^2(k)$ is Gaussian and has a center wavelength of 830 nm and a bandwidth of 340 nm. The simulated lens has a focal length of 10 mm, a spot size of 4 μm, and a confocal parameter of 30 μm corresponding to a NA of 0.2. These parameters correspond to a NA and bandwidth larger than usually encountered in OCT systems to enable exploration of the full potential of the algorithm to work in regions of large distortion.

The steps involved in the forward simulations are described in Table 2. The thin-sample approximation is used to generate an OCT signal $S_k(\mathbf{r}_0, k)$ from the synthetic object $\eta(\mathbf{r}_0; z)$. The fast Fourier transform (FFT) of the two-dimensional susceptibility of the object is given by $\tilde{\eta}(\mathbf{Q}; \beta)$, where $\mathbf{Q}$ is the transverse and β is the axial spatial-frequency coordinate. The forward integral operator K, from Eq. (3.1) and implicit in Eq. (4.8), is used to generate $\tilde{S}(\mathbf{Q}, k)$ from $\tilde{\eta}(\mathbf{Q}; \beta)$. Explicitly, an interpolator must be chosen to make a coordinate transformation from coordinates that are spaced uniformly in β to coordinates that are spaced uniformly in k. We used cubic B-spline interpolation preceded by sinc interpolation, which is used to double the number of data points and increase the cubic B-spline accuracy.[26] Next, multiplying by the square root of the spectrum $A(k)$ ($\Delta\lambda = 340$ nm) with cutoffs at π/λ_{max} and π/λ_{min} simulates the coherence gating, which defines the axial resolution for the system. Finally, the factor $I_k(\mathbf{Q}, k) = k^2 e^{-Q^2\alpha^2/(4k^2)}/(4\pi\alpha^2)$ is applied to obtain $\tilde{S}(\mathbf{Q}, k)$. The inverse FFT (IFFT) of $\tilde{S}(\mathbf{Q}, k)$ is taken in the transverse direction to recover the OCT signal $S(\mathbf{r}_0, k)$.

The method for calculating $S_t(\mathbf{r}_0, t)$, as seen in Fig. 5(b) from $S_k(\mathbf{r}_0, k)$ is described in Table 3. For simplicity, we assume the dispersion relation $k = k(\omega)$. Table 4 shows the calculation of $S_k(\mathbf{r}_0, k)$ from $S_t(\mathbf{r}_0, t)$.

Gaussian white noise is added to the signal $S_t(\mathbf{r}_0, t)$ to simulate two different SNRs, 35 and -5 dB. A noisy version of the simulated digitized signal is generated,

$$S_n = S_t(\mathbf{r}_0, t) + n, \tag{5.1}$$

where n is a random variable from a set of independent, identically distributed Gaussian noise samples with probability distribution

$$P(n) = \frac{1}{\sigma_n\sqrt{2\pi}}e^{-n^2/(2\sigma_n^2)}. \tag{5.2}$$

The SNR is the ratio of the mean squared signal σ_S^2 across the whole data set to the variance of the noise σ_n^2 according to the following equation:

$$\text{SNR(dB)} = 10 \log_{10}(\sigma_S^2/\sigma_n^2). \tag{5.3}$$

Thus

$$\sigma_n = \sqrt{\sigma_s/10^{SNR/10}}. \tag{5.4}$$

The standard deviation of the noise σ_n was determined for a SNR of 35 dB, which is less than the typical dynamic range for data contained within an OCT image, and an image was also created with an SNR of −5 dB, which is noisier than typical for OCT so as to demonstrate the robustness of the algorithm. Testing algorithms with extremes of SNR serves to evaluate the algorithm performance and determine useful regularization parameters. The OCT images generated from the forward model and the addition of Gaussian white noise are shown in Figs. 5 and 6. The field of view for the simulated OCT images is truncated on the left and right before reconstruction to include the effects of scatterers that lie outside of the imaged coherence volume. These scatterers scatter into the field of view due to the finite beam width.

Table 5 describes the procedure, using the thin-sample approximation, for generating the unfiltered solution $\eta_A(\mathbf{r}_0;z)$ from $S(\mathbf{r}_0,k)$. The FFT of the two-dimensional signal $S(\mathbf{r}_0,k)$ is given by $\widetilde{S}(\mathbf{Q},k)$, where $\mathbf{Q}$ is the transverse wave vector. The adjoint operator K^*, seen in Eq. (4.2) and implicit in Eq. (4.9), is used to generate the unfiltered solution $\widetilde{\tilde{\eta}}_A(\mathbf{Q};\beta)$ from $\widetilde{S}(\mathbf{Q},k)$. Specifically, we multiply $\widetilde{S}(\mathbf{Q},k)$ with $A(k)$, $I_k(\mathbf{Q},k)$, and the Jacobian $|2$

$+Q^2/4k^2|^{-1}$. Then to solve for $\widetilde{\tilde{\eta}}_A(\mathbf{Q};\beta)$, an interpolator is chosen to make a coordinate transform from coordinates that are spaced uniformly in k to coordinates that are spaced uniformly in β. The IFFT of $\widetilde{\tilde{\eta}}_A(\mathbf{Q};\beta)$ is taken in the axial and transverse directions to recover the unfiltered object susceptibility $\eta_A(\mathbf{r}_0;z)$.

The Tikhonov method is used to regularize the solution. Figures 7 and 8 show the unfiltered solution $\eta_A(\mathbf{r}_0;z)$ and the regularized $\hat{\eta}(\mathbf{r}_0;z)$ solutions for each SNR value. The calculation of the regularized solution $\hat{\eta}(\mathbf{r}_0;z)$ from the unfiltered solution $\eta_A(\mathbf{r}_0;z)$ using the thin-sample approximation is outlined in Table 6. The FFT of $\eta_A(\mathbf{r}_0;z)$ is

Table 5. Steps in the Calculation of $\eta_A(\mathbf{r}_0;z)$ from $S(\mathbf{r}_0,k)$ Using the Thin-Sample Approximation

1. FFT $S(\mathbf{r}_0,k)$ along the transverse direction $\mathbf{r}_0$ to obtain $\widetilde{S}(\mathbf{Q},k)$.
2. Apply a filter to $\widetilde{S}(\mathbf{Q},k)$, multiplying by $I_k(\mathbf{Q},k) = k^2\, e^{-Q^2\alpha^2/(4k^2)}/(4\pi\alpha^2)$, $-iA(k)$, and $|2+Q^2/4k^2|^{-1}$.
3. Interpolate samples uniform in k to samples uniform in β using the relation $k = (\beta/2 + \sqrt{(\beta/2)^2 + Q^2/2})/2$ to find $\widetilde{\tilde{\eta}}_A(\mathbf{Q};\beta)$.
4. IFFT $\widetilde{\tilde{\eta}}_A(\mathbf{Q};\beta)$ along the transverse and axial directions to obtain $\eta_A(\mathbf{r}_0;z)$.

(a)   **(b)**

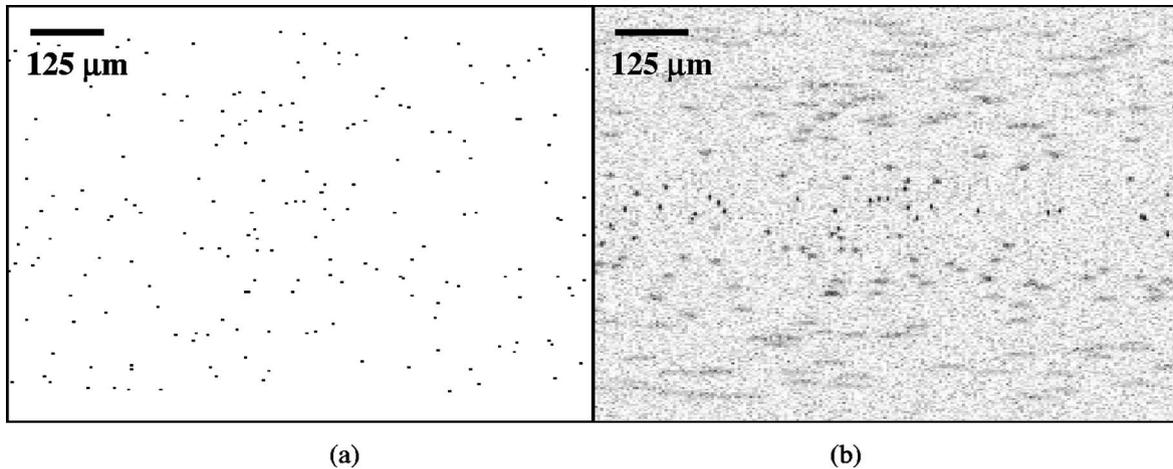Fig. 6.   (a) Original object model of point scatterers and (b) simulated OCT image with SNR=−5 dB.

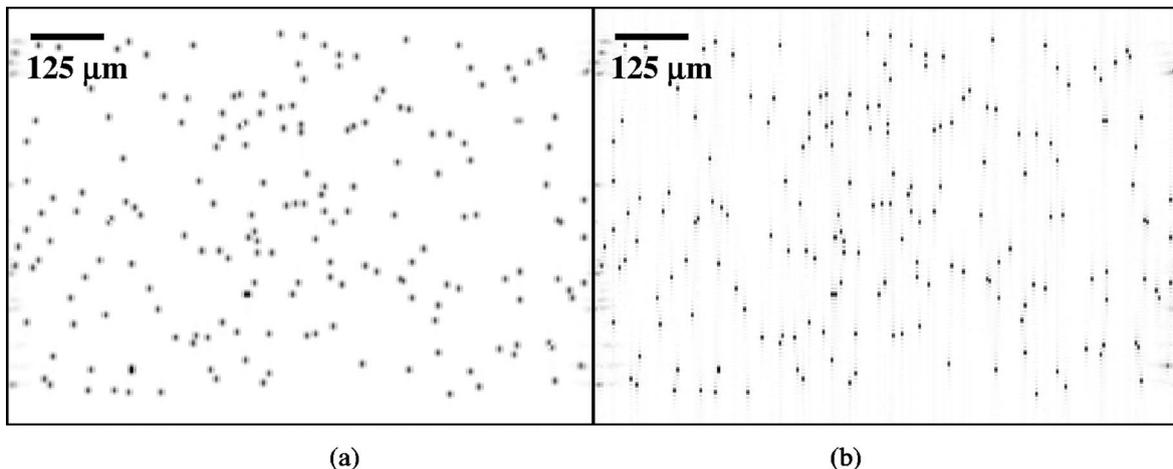**(a)**   **(b)**

Fig. 7.   (a) Unfiltered reconstruction and (b) Tikhonov regularized solution, λ=60, for SNR values of 35 dB.
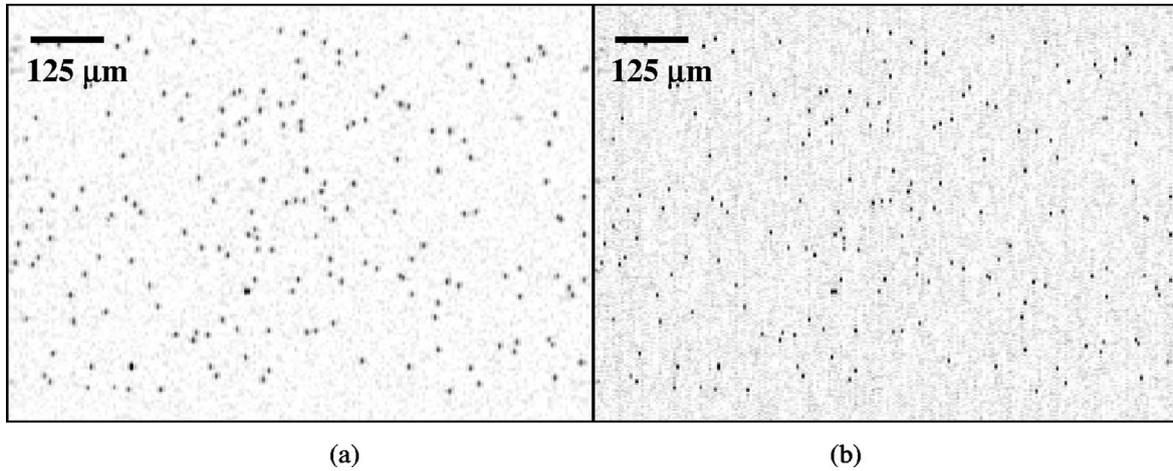
Fig. 8. (a) Unfiltered reconstruction and (b) Tikhonov regularized solution, $\lambda = 60$, for SNR values of -5 dB.

Table 6. Steps in the Calculation of $\hat{\eta}(\mathbf{r}_0; z)$ from $\eta_A(\mathbf{r}_0; z)$ Using the Thin-Sample Approximation

1. FFT $\eta_A(\mathbf{r}_0; z)$ along the transverse and axial directions to obtain $\tilde{\tilde{\eta}}_A(\mathbf{Q}; \beta)$.

2. Apply a filter to $\tilde{\tilde{\eta}}_A(\mathbf{Q}; \beta)$, multiplying by $(\lambda + I_k(\mathbf{Q}, k)^2 A(k)^2 / |2 + Q^2/4k^2|)^{-1}$, where $I_k(\mathbf{Q}, k)^2 = (k^2 \, e^{-Q^2 \alpha^2/(4k^2)}/(4\pi\alpha^2))^2$ and $k = (\beta/2 + \sqrt{(\beta/2)^2 + Q^2/2})/2$.

3. IFFT the filtered $\tilde{\tilde{\eta}}_A(\mathbf{Q}; \beta)$ along the axial and transverse directions to yield $\hat{\eta}(\mathbf{r}_0; z)$.

taken in the transverse and axial directions to obtain object susceptibility in spatial-frequency coordinates $\tilde{\tilde{\eta}}_A(\mathbf{Q}; \beta)$. The regularized inverse of the normal operator $(K^*K + \lambda I)^{-1}$ is used to generate $\hat{\tilde{\tilde{\eta}}}(\mathbf{Q}; \beta)$ from $\tilde{\tilde{\eta}}_A(\mathbf{Q}; \beta)$. To choose an appropriate regularization parameter, λ, the L-curve method[23] is typically used to balance the weights of the seminorm $\|Lx\|_2$ and the residual norm $\|Ax - b\|_2$. Several values for the regularization parameter were explored, and a value $\lambda = 60$ was found to balance appropriately the norms when L is taken to be the identity. Smaller values for λ cause the artifacts above and below the scatterers to be emphasized. The regularized filter and $I_k(\mathbf{Q}, k)^2$ are multiplied with $\tilde{\tilde{\eta}}_A(\mathbf{Q}; \beta)$. Finally, the IFFT is taken in both the axial and the transverse directions to yield $\hat{\eta}(\mathbf{r}_0; z)$.

6. CONCLUSION

In this work, a comprehensive model for OCT has been presented for which forward, adjoint, normal, and inverse operators were formulated. These results suggest that accurate linear estimation of the susceptibility of an object from OCT data is possible given an accurate model for the probe beam. Using the regularized least-squares solution, we have obtained in simulation a reconstruction of underlying object structure with spatially invariant resolution from simulated OCT images covering regions outside of the focus. Two- and three-dimensional OCT data can be used to resolve objects outside of the confocal region with minimal loss of resolution. High-resolution details can be recovered from outside of the confocal region. The model

presented accounts for the effects of a finite beam width, the source spectrum, as well as defocus, diffraction, and dispersion effects.

A number of directions for further research are apparent. Vignetting attributable to the finite pupil of any realistic optical system might be taken into account in the forward model. Background structure of the sample, if known *a priori*, may be included through modification of the Green's function. For example, if the medium is known to have a layered structure, then prior knowledge may be included in the forward and inverse problems by replacing the free-space Green's function with one for stratified media. Furthermore, polarization effects might be taken into account by rederiving the results making use of a vector electric field and dyadic Green's function. Most importantly these results must be confirmed by experiment. Efforts are ongoing, with promising early results.

APPENDIX A

The field at the output face of the fiber is given by $U_i(\mathbf{r})|_{z=0} = A(k)\phi(\mathbf{r})$. The field propagates to the plane $z = z_\ell$ where a thin lens is located. To the left of the $z = z_\ell$ plane, the field is given by the expression

$$U_i(\mathbf{r}) = A(k) \int d^2 r' P(\mathbf{r}, \mathbf{r}') \phi(\mathbf{r}'), \qquad (A1)$$

where $P(\mathbf{r}, \mathbf{r}')$ is the free-space diffraction kernel. The lens is assumed to be a thin phase screen with the transfer function given by $L(\mathbf{r})$, see Fig. 9. Thus just to the right of the lens ($z = z_\ell$) the field is given by $U_i(\mathbf{r}) = A(k)L(\mathbf{r}) \int d^2 r' P(\mathbf{r}, \mathbf{r}') \phi(\mathbf{r}')$. The field is focused into a Gaussian beam with beam waist in the $z = z_0$ plane. The field is given by the expression $U_i(\mathbf{r}) = A(k)g(\mathbf{r})$. Thus the normalized beam profile is also given by the expression

$$g(\mathbf{r}) = \int_{z'=z_\ell} d^2 r' L(\mathbf{r}') \int_{z''=0} d^2 r'' P(\mathbf{r}', \mathbf{r}'') \phi(\mathbf{r}'') P(\mathbf{r}, \mathbf{r}').$$

$$(A2)$$

The coupling of light back into the fiber is now derived in terms of the normalized waist plane field $g_0(\mathbf{r})$ given in
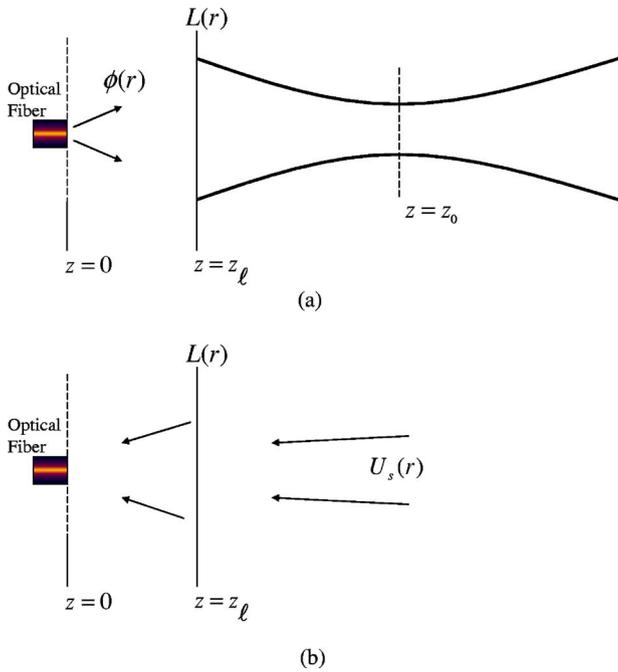
Fig. 9.   (Color online) Illustration of the coupling of light (a) out of and (b) into the fiber.

Eqs. (3.3) and (A2). Consider a field that propagates back toward the fiber and is given in some plane Σ by $U_s(\mathbf{r})$ on the right side of the lens. The field may be propagated to the lens where it acquires the factor $L(\mathbf{r})$. The field incident on the fiber face $U_s(\mathbf{r})|_{z=z_0}$ will then be given by the expression

$$U_s(\mathbf{r})|_{z=0} = \int_{z'=z_\ell} d^2 r' P(\mathbf{r},\mathbf{r}') L(\mathbf{r}') \int_{\Sigma} d^2 r'' P(\mathbf{r}',\mathbf{r}'') U_s(\mathbf{r}'').$$
(A3)

The signal coupled into the single-mode fiber is then given by the inner product of this field [Eq. (A3)] and the fiber mode $\phi(\mathbf{r})$,

$$S = \int_{z=0} d^2 r\, \phi^*(\mathbf{r}) U_s(\mathbf{r}).$$
(A4)

Equations (A3) and (A4) may be combined to yield

$$S = \int_{z=0} d^2 r \phi^*(\mathbf{r}) \int_{z'=z_\ell} d^2 r' P(\mathbf{r},\mathbf{r}') L(\mathbf{r}')$$
$$\times \int_{\Sigma} d^2 r'' P(\mathbf{r}',\mathbf{r}'') U_s(\mathbf{r}'').$$
(A5)

The field emerging from the fiber is assumed to be a diverging Gaussian beam with a beam waist at $z=0$. Thus $\phi^*(\mathbf{r})=\phi(\mathbf{r})$. By comparing Eqs. (A2) and (A5) and noting that $P(\mathbf{r}'',\mathbf{r}')=P(\mathbf{r}',\mathbf{r}'')$, it may be seen that

$$S = \int_{\Sigma} d^2 r\, g(\mathbf{r}) U_s(\mathbf{r}).$$
(A6)

This is the expression for the signal used in the paper.

REFERENCES

1. P. S. Cooper, A. F. Wons, and A. P. Gaskell, "High resolution synthetic aperture radar using a multiple sub-band technique," in *IEEE Proceedings of Radar Systems*, Conf. Publ. 449 (IEEE Press, 1997), pp. 263–267.
2. R. Lanari, S. Zoffoli, E. Sansosti, G. Fornaro, and F. Serafino, "New approach for hybrid strip-map/spotlight SAR data focusing," IEE Proc., Radar Sonar Navig. **148**, 363–372 (2001).
3. D. Huang, E. A. Swanson, C. P. Lin, J. S. Schuman, W. G. Stinson, W. Chang, M. R. Hee, T. Flotte, K. Gregory, C. A. Puliafito, and J. G. Fujimoto, "Optical coherence tomography," Science **254**, 1178–1181 (1991).
4. J. M. Schmitt, "Optical coherence tomography (OCT): a review," IEEE J. Sel. Top. Quantum Electron. **5**, 1205–1215 (1999).
5. B. E. Bouma and J. G. Tearney, eds., *The Handbook of Optical Coherence Tomography* (Marcel Dekker, 2001).
6. M. E. Brezinski, G. J. Tearney, S. A. Boppart, E. A. Swanson, J. F. Southern, and J. G. Fujimoto, "Optical biopsy with optical coherence tomography: feasibility for surgical diagnostics," J. Surg. Res. **71**, 32–40 (1997).
7. S. A. Boppart, W. Luo, D. L. Marks, and K. W. Singletary, "Optical coherence tomography: feasibility for basic research and image-guided surgery of breast cancer," Breast Cancer Res. Treat. **84**, 85–97 (2004).
8. L. K. Jensen, L. Thrane, P. E. Andersen, A. Tycho, F. Pedersen, S. Andersson-Engels, N. Bendsoe, S. Svanberg, and K. Svanberg, "Optical coherence tomography in clinical examinations of nonpigmented skin malignancies," in *Optical Coherence Tomography and Coherence Techniques*, W. Drexler, ed., Proc. SPIE **5140**, 160–167 (2003).
9. B. Hermann, E. J. Fernandez, A. Unterhuber, H. Sattmann, A. F. Fercher, W. Drexler, P. M. Prieto, and P. Artal, "Adaptive-optics ultrahigh-resolution optical coherence tomography," Opt. Lett. **29**, 2142–2144 (2004).
10. Z. Ding, H. Ren, Y. Zhao, J. S. Nelson, and Z. Chen, "High-resolution optical coherence tomography over a large depth range with an axicon lens," Opt. Lett. **27**, 243–245 (2002).
11. Y. Wang, Y. Zhao, J. S. Nelson, and Z. Chen, "Ultrahigh-resolution optical coherence tomography by broadband continuum generation from a photonic crystal fiber," Opt. Lett. **28**, 182–184 (2003).
12. M. J. Cobb, X. Liu, and X. Li, "Continuous focus tracking for real-time optical coherence tomography," Opt. Lett. **30**, 1680–1682 (2005).
13. M. D. Kulkarni, C. W. Thomas, and J. A. Izatt, "Image enhancement in optical coherence tomography using deconvolution," Electron. Lett. **33**, 1365–1367 (1997).
14. D. L. Marks, A. L. Oldenburg, J. J. Reynolds, and S. A. Boppart, "Digital algorithm for dispersion correction in

optical coherence tomography for homogeneous and stratified media," Appl. Opt. **42**, 204–217 (2003).

15. T. Blu, H. Bay, and M. Unser, "A new high-resolution processing method for the deconvolution of optical coherence tomography signals," presented at the IEEE International Symposium on Biomedical Imaging, Washington, D.C., July 7–11, 2002.

16. O. Bruno and J. Chaubell, "One-dimensional inverse scattering problem for optical coherence tomography," Inverse Probl. **21**, 499–524 (2005).

17. O. Bruno and J. Chaubell, "Inverse scattering problem for optical coherence tomography," Opt. Lett. **28**, 2049–2051 (2003).

18. A. Podoleanu, I. Charalambous, L. Plesea, A. Dogariu, and R. Rosen, "Correction of distortions in optical coherence tomography imaging of the eye," Phys. Med. Biol. **49**, 1277–1294 (2004).

19. Y. Feng and R. K. Wang, "Theoretical model of optical coherence tomography for system optimization and characterization," J. Opt. Soc. Am. A **20**, 1792–1803 (2003).

20. A. F. Fercher, C. K. Hitzenberger, G. Kamp, and S. Y. El-Zaiat, "Measurement of intraocular distances by backscattering spectral interferometry," Opt. Commun. **117**, 43–48 (1995).

21. J. F. deBoer, B. Cense, B. H. Park, M. C. Pierce, G. J. Tierney, and B. E. Bouma, "Improved signal-to-noise ratio in spectral-domain compared with time-domain optical coherence tomography," Opt. Lett. **28**, 2067–2069 (2003).

22. J. A. Izatt, M. R. Hee, G. M. Owen, E. A. Swanson, and J. G. Fujimoto, "Optical coherence microscopy in scattering media," Opt. Lett. **19**, 590–592 (1994).

23. L. Mandel and E. Wolf, *Optical Coherence and Quantum Optics* (Cambridge U. Press, 1995), p. 1192.

24. R. Courant and D. Hilbert, *Methods of Mathematical Physics* (Wiley-Interscience, 1989), pp. 142–147.

25. P. C. Hansent, "Numerical tools for analysis and solution of Fredholm integral equations of the first kind," Inverse Probl. **8**, 849–872 (1992).

26. C. Pozrikidis, *Numerical Computation in Science and Engineering* (Oxford U. Press, 1998), pp. 406–408.